nature catalysis

SUPPLEMENTARY INFORMATION

https://doi.org/10.1038/s41929-018-0169-3

In the format provided by the authors and unedited.

Detection of catalytic intermediates at an electrode surface during carbon dioxide reduction by an earth-abundant catalyst

Gaia Neri[1], James. J. Walsh[1,4], Gilberto Teobaldi[1,2,5], Paul M. Donaldson[3]* and Alexander J. Cowan[1]*

[1]Department of Chemistry and Stephenson Institute for Renewable Energy, University of Liverpool, Liverpool, UK. [2]Beijing Computational Science Research Center, Beijing, China. [3]Central Laser Facility, STFC Rutherford Appleton Laboratory, Didcot, Oxfordshire, UK. [4]Present address: School of Chemical Sciences and National Centre for Sensor Research, Dublin City University, Dublin , Ireland. [5]Present address: Scientific Computing Departmet, STFC Daresbury Laboratory, Daresbury, UK. *e-mail: paul.donaldson@stfc.ac.uk; acowan@liverpool.ac.uk

Detection of catalytic intermediates at an electrode surface during carbon dioxide reduction by an earth-abundant catalyst

Gaia Neri,[a] James. J. Walsh[a ‡], Gilberto Teobaldi,[a,b] Paul M. Donaldson[c] and Alexander J. Cowan[a *]*

[a]Department of Chemistry and Stephenson Institute for Renewable Energy, University of Liverpool, L69 7ZD, Liverpool, UK, acowan@liverpool.ac.uk,

[b]Beijing Computational Science Research Center 100193 Beijing, China

[c]Central Laser Facility, STFC Rutherford Appleton Laboratory, Harwell, Didcot, Oxfordshire, OX11 0QX, UK, paul.donaldson@stfc.ac.uk

[‡]Current address, School of Chemical Sciences and National Centre for Sensor Research, Dublin City University, Glasnevin, Dublin 9, Ireland

Supplementary methods

The deviation from the classical peak shapes typically observed for freely diffusing species in figure 1 (main text) is due to the short distance between the electrode surface and the cell front window (50 μm). Variable scan rate CVs recorded on the same Au-Hg electrodes in a standard electrochemical cell do not show such behaviour and the-scan rate dependence of peak current indicates the presence of freely diffusing species in solution, supplementary figure 1.

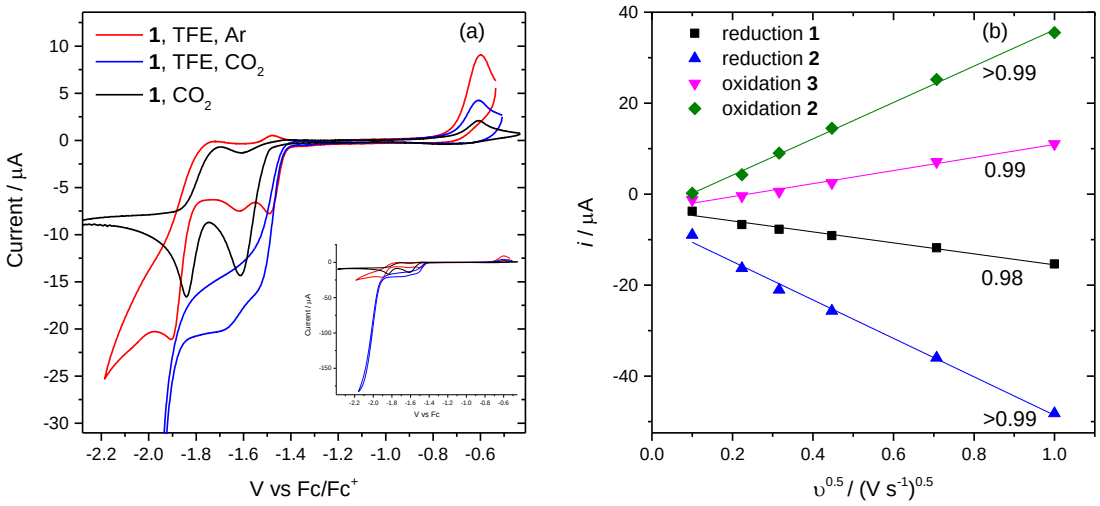

*Supplementary Figure 1. (a) CV of **1** (1 mM) recorded in a pear shaped flask using a Au-Hg working electrode, Pt counter electrode and Ag pseudo reference electrode. CV recorded at 100 mVs^{-1} in CH_3CN and 0.1 M $TBAPF_6$ under the conditions indicated, TFE when present is at 1.5 M. The right hand side (b) shows the expected scan rate-peak current dependence relationship of a freely diffusing species in solution. The values stated in (b) are the R^2 of the fit lines.*

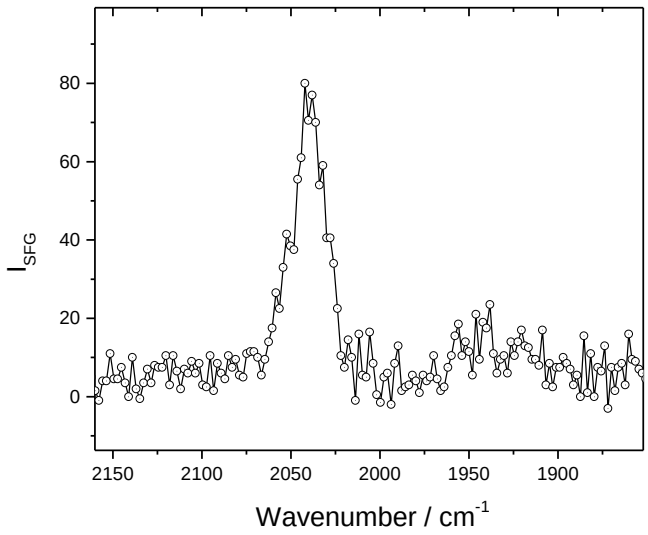

*Supplementary Figure 2: VSFG spectrum of **1** (1 mM) at the Au-Hg electrode surface (0.1 V) in CH_3CN, 0.1 M $TBAPF_6$, TFE (1.5 M) under an argon atmosphere.*

VSFG of molecules at the electrode surface: It is possible to observe VSFG of molecular electrocatalysts as for electron transfer to occur molecules are either specifically adsorbed onto the electrode surface (sometimes called inner-sphere electron transfer) or electron transfer takes place when the molecule is close to the surface, often at the outer-Helmholtz plane (OHP, outer-sphere electron transfer). Therefore electron transfer only takes place from the electrode to species within the electrode double layer (EDL) structure – Faradaic processes are heterogeneous reactions.[5] Molecules within the EDL will be subject to very large electric fields – the entire double layer structure will typically be on the order of a few nm across so fields and ~10^7-10^8 V cm^{-1} are feasible for molecules at the OHP, whilst ~10^9 V cm^{-1} can occur for specifically adsorbed molecules. Therefore ordering and structuring of molecules within the EDL occurs and the concentration of the electroactive species (particularly charged species) can increase. This is observed in the main text (figure 2) during VSFG studies of CV experiments where we see species accumulate at the electrode, with intensity of the VSFG signals reaching a maximum immediately prior to the point where we start to observe the flow of current. As current flows, indicating either the oxidation or reduction of the complex we observe a decrease in the intensity of the VSFG signal demonstrating that we are following the decrease in concentration of the complex at/close to the electrode surface.

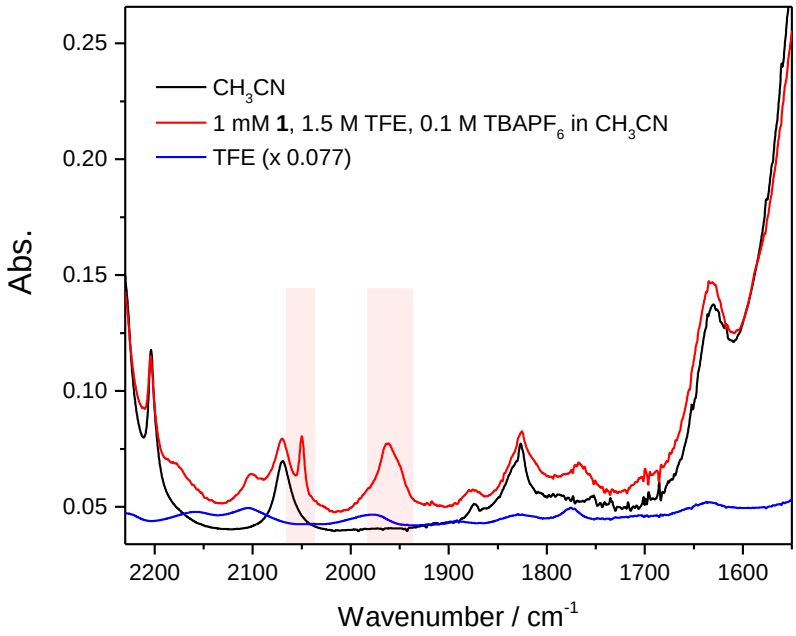

*Supplementary Figure 3: Solution FTIR spectrum (air background), 50 μm pathlength of **1** (1 mM) in CH_3CN, 0.1 M $TBAPF_6$, 1.5 M TFE (red). Spectra of neat TFE (13 M) scaled by x0.077, and CH_3CN (both 50 μm pathlength) are also included for reference. The ν(CO) bands of **1** are highlighted by pale red boxes.*

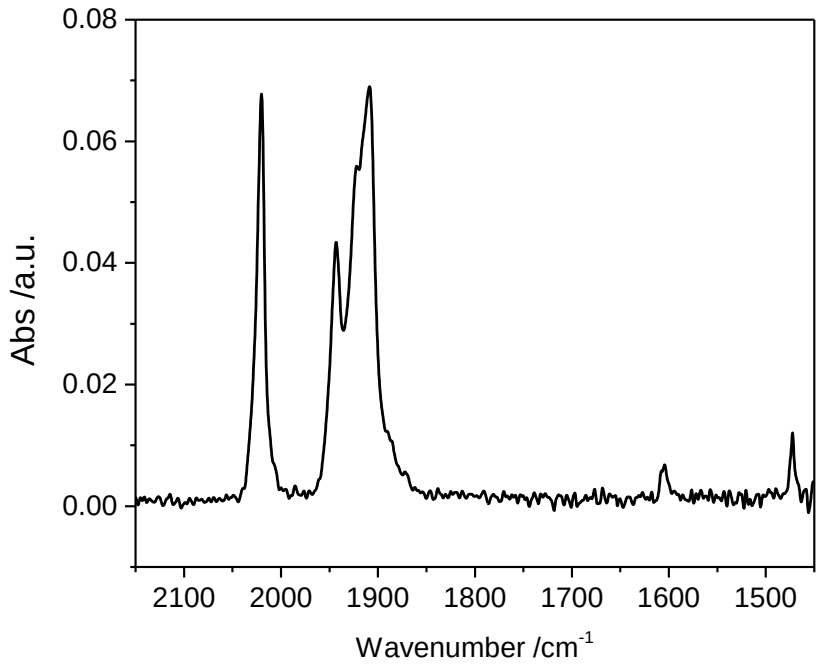

Supplementary Figure 4: FTIR-ATR spectrum of $Mn(bpy)(CO)_3Br$ (solid) showing the presence of the bipyridine mode at 1605 cm^{-1}

Complex	ν(CO) / cm^{-1}	Solvent	Reference
1	2045, 1965 1953	CH_3CN	[1]
2	1973, 1927, 1880, 1849	CH_3CN	[2]
3	1911, 1811	CH_3CN	[3]
4	1991, 1892, 1888 (*sh*)	CH_3CN	[3]
5	*unknown*		
6	*unknown*		
7	*unknown*		
8	2118, 2044, 2023, 1982	CH_2Cl_2	[4]
9	*unknown*		
10	*unknown*		

Supplementary Table 1: Literature values for ν(CO) modes of relevant complexes in solution recorded by IR spectroscopy.

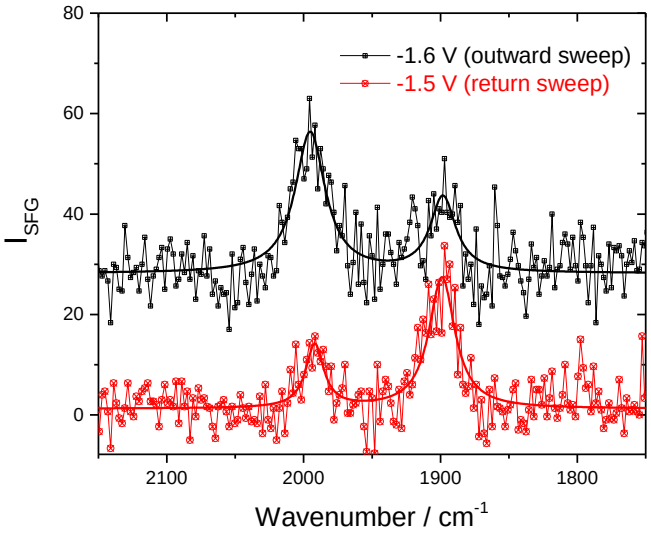

*Supplementary Figure 5: Individual VSFG spectra at the single voltages indicated during the CV of **1** (1 mM) in CH_3CN (0.1 M $TBAPF_6$) and 1.5 M TFE under Ar showing the presence of the hydride, $[Mn(bpy)(CO)_3H]$, **4**. Red and black lines show the result of a multi-Lorentzian fit.*

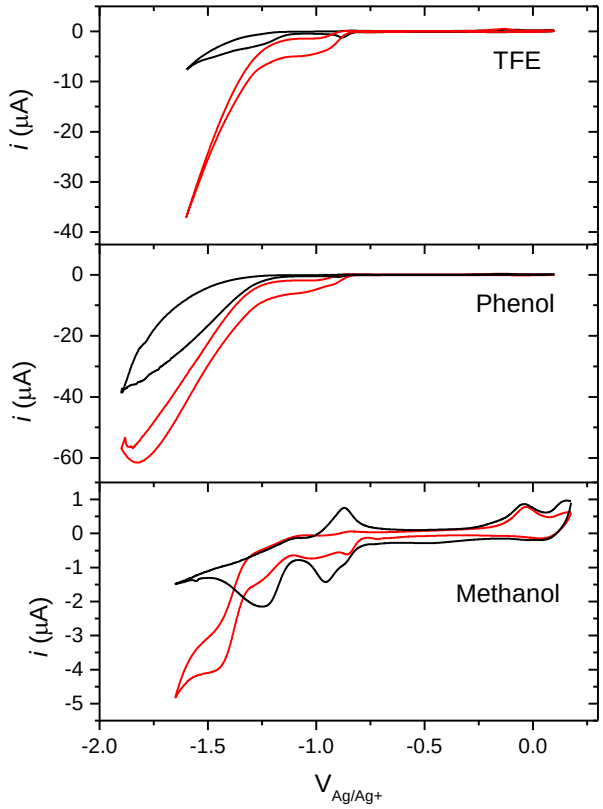

*Supplementary Figure 6: CVs of **1** (1 mM) recorded within the SEC cell at 10 mVs^{-1} during VSG experiments in CH_3CN and 0.1 M $TBAPF_6$ under the conditions indicated, TFE, phenol and methanol are at 1.5 M. CV's recorded under Ar (black) or CO_2 (red).*

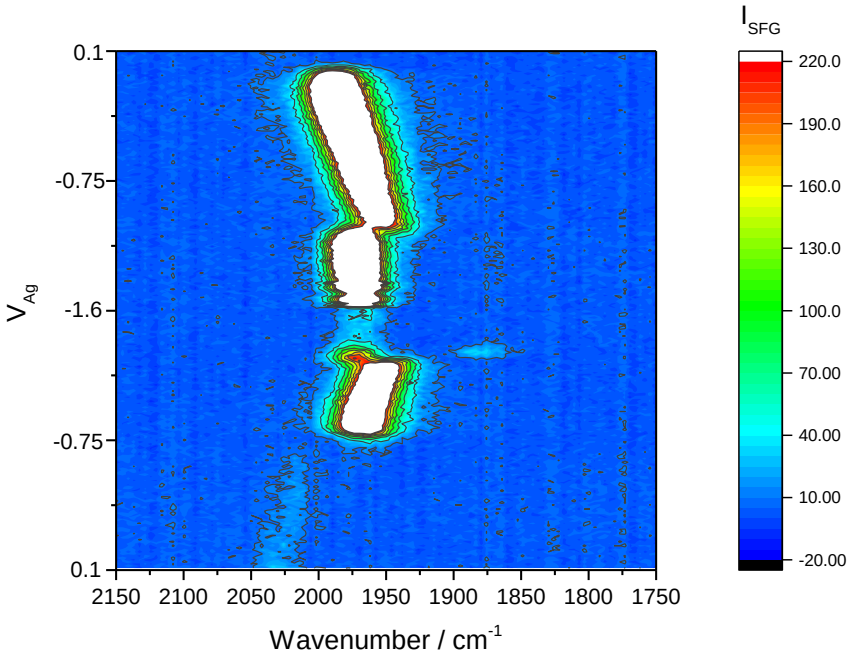

*Supplementary Figure 7: VSFG spectra recorded during CV's (10 mV s^{-1}) of **1** (1 mM) in CH_3CN (0.1 M $TBAPF_6$) and 1.5 M TFE under CO_2 with the IR pulse centred at ~1950 cm^{-1}. The spectrum is zoomed into to highlight the lack of a ν(CO) band at 1898 cm^{-1} or 1994 cm^{-1} that could be assigned to **4** when CO_2 is present. Instead only features relating to CO_2 reduction intermediates at ca. 1976, 1600 and 1875 cm^{-1} are observed between -1.2 and -1.6 V.*

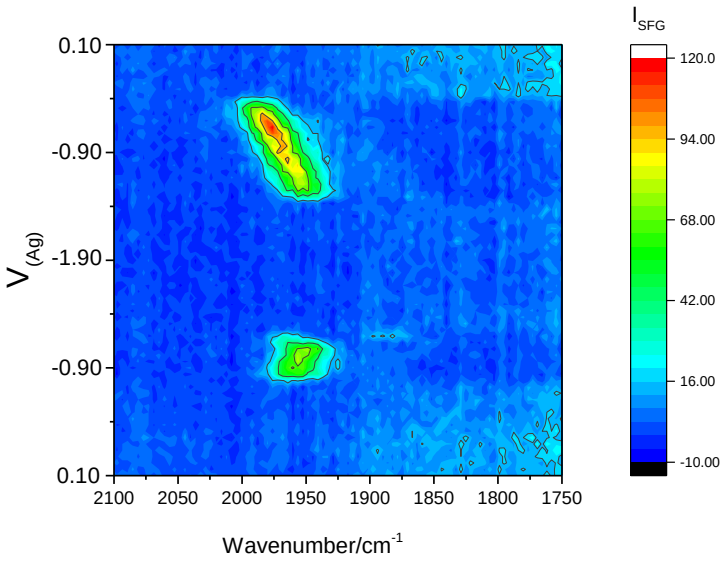

*Supplementary Figure 8: VSFG spectra recorded during CV's (10 mV s^{-1}) of **1** (1 mM) in CH_3CN (0.1 M $TBAPF_6$) under CO_2 in the absence of a deliberately added acid source.*

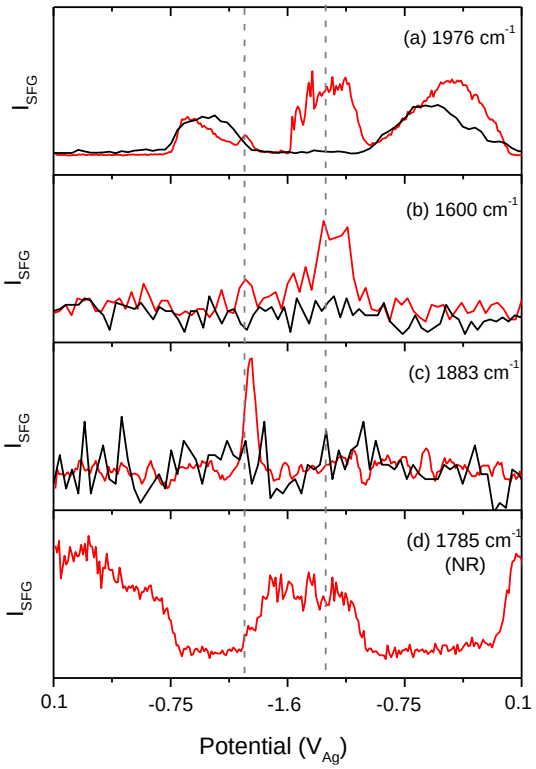

*Supplementary Figure 9: Intensity of the SFG signal during CV's (10 mV s^{-1}) of **1** (1 mM) in CH_3CN (0.1 M $TBAPF_6$) and 1.5 M TFE under CO_2 (red) and Ar (black). (a-c) are the resonant VSFG responses recorded with a 0.9 ps delay between the IR and Vis laser pulses at the wavenumber indicated. (d) is recorded with 0 ps delay between the IR and Vis laser pulses at a wavelength where no strong resonant VSFG bands are expected and is a measure of the non-resonant SFG signal with applied potential. The dotted lines highlight the potentials where the new intermediate species (**8**) is observed.*

Supplementary figure 9 shows that the new VSFG bands present under CO_2 at 1976 cm^{-1} and 1600 cm^{-1} have the same potential dependence indicating that they are from a common species at the electrode surface, assigned in the main text to **8**. They only appear under CO_2 and in the presence of a stronger (phenol, TFE) acid indicating that they are likely to be intermediates on the protonation first CO_2 reduction pathway. An additional band relating to CO_2 reduction at 1883 cm^{-1} is also present. This forms following the loss of the VSFG bands of **8** on the outward CV sweep and it is likely to be due to a different species at the surface. We can rule out that the VSFG bands assigned to **8** could be assigned to a phantom transition as there is no correlation between the I_{SFG} at 1600 cm^{-1} and 1976 cm^{-1} and the non-resonant signal[6] arising from the electrode surface and species within the double layer.

The VSFG band at 1600 cm^{-1} observed in the main text (figure 4) and shown above in supplementary figure 9 is assigned to a bipyridine (bpy) mode of **8**. This is on the basis of the excellent correlation with the observed wavenumber of the bpy mode (1600 cm^{-1}) and that calculated for the bpy fragment of **8** on the Hg surface (1594 cm^{-1}) and in vacuum (1599 cm^{-1}), see supplementary table 4 below. Benchmark calculations of **1** in vacuum (1599 cm^{-1}) are in excellent agreement with the experimental measurement of 1604 cm^{-1} (CH_2Cl_2 solution) and 1605 cm^{-1} (solid). Other potential assignments considered for the VSFG band at 1600 cm^{-1} included to water (evolved during CO_2 reduction, see main text figure 1), Mn-CO_2 adducts (including Mn-CO_2H) and the reaction product of the TFE alkoxide with CO_2 ($[F_3CCH_2OCO_2]^-$). However the lack of shift in the SFG spectrum upon the use of $^{13}C^{18}O_2$ allows us to exclude these assignments.

VSFG bands corresponding to bipyridine modes can also be observed for other species in our experiments (e.g. **1**, **4**). In many of the experiments the focus was on the ν(CO) region therefore the IR intensity of was centred at ~2000 cm^{-1} and the bpy modes (~1600 cm^{-1}) would not be detectable. However in figure 4 of the main text we centred the IR intensity to 1750 cm^{-1} to allow for the study of both the bpy and ν(CO) regions. Supplementary figure 10 shows a version of figure 4(a), zoomed in, to allow for the observation of the bpy modes which are clearly present when species **1** and **4** are at the electrode. We have not observed bpy modes for **2** to date but it is important to note that the frequency of bpy vibrational modes are known to be sensitive to the electron density at the metal centre and this is demonstrated in the calculations below where they shift by ~50 cm^{-1} between complexes **6**-**9**. Therefore it is feasible that they are beyond our spectral window (below 1580 cm^{-1} acetonitrile is strongly absorbing).

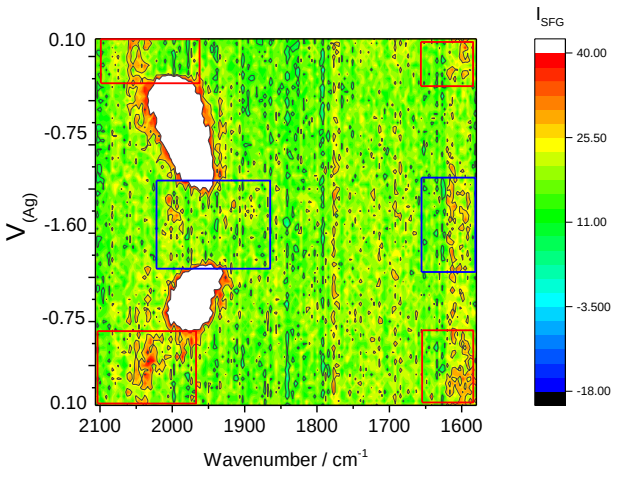

*Supplementary Figure 10: VSFG spectra recorded during CV (10 mV s^{-1}) of **1** (1 mM) in CH_3CN (0.1 M $TBAPF_6$) and 1.5 M TFE under Ar with the IR pulse centred at ~1750 cm^{-1}. The spectrum is zoomed in to highlight the bpy modes of **1** and **4**. The ν(CO) and bpy modes are highlighted with red (**1**) and blue (**4**) boxes.*

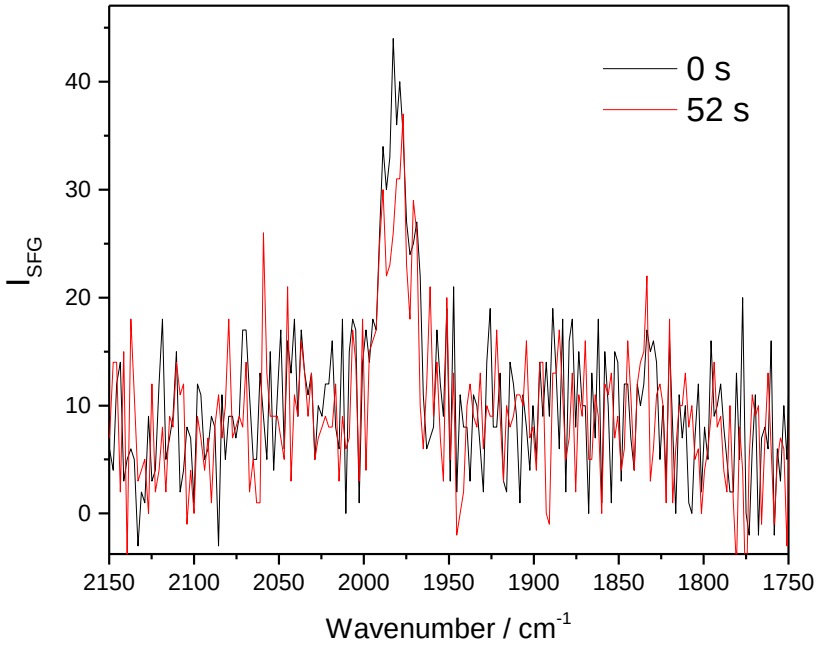

*Supplementary Figure 11: VSFG spectra recorded of **1** (1 mM) in CH_3CN (0.1 M $TBAPF_6$) and 1.5 M TFE under CO_2. A CV is carried out at 50 mV s^{-1} between 0.1 and -1.6 V_{Ag} and the potential held at ca. -1.4 V for approximately 1 minute. During this period we see no discernible decrease in intensity of the ν(CO) SFG mode assigned to **8**.*

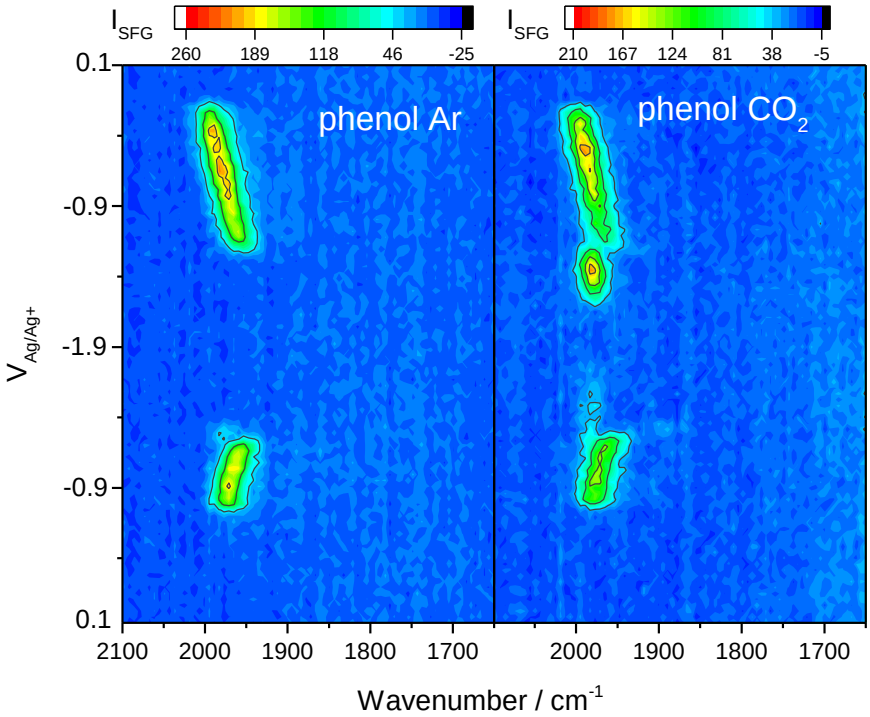

*Supplementary Figure 12: VSFG spectra recorded during CV (10 mV s^{-1}) of **1** (1 mM) in CH_3CN (0.1 M $TBAPF_6$) under Ar and CO_2 in the presence of 1.5 M phenol. The recording of VSFG spectra at wavenumbers below 1650 cm^{-1} was not possible due to the strong phenol modes that led to significant IR absorption by the electrolyte solution in this region.*

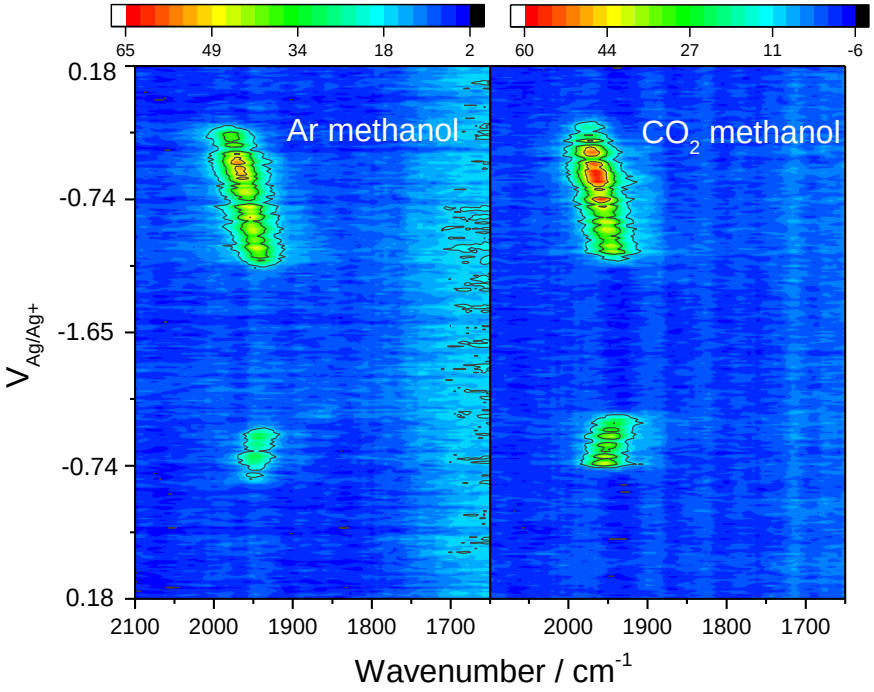

*Supplementary Figure 13: VSFG spectra recorded during CV (10 mV s^{-1}) of **1** (1 mM) in CH_3CN (0.1 M $TBAPF_6$) under Ar and CO_2 in the presence of 1.5 M methanol.*

Using methanol as the acid source it is widely predicted, and our CV data also indicates, that the protonation first pathway does not operate. **8** is only formed by the protonation first pathway, in contrast **9** is common to all predicted CO_2 reduction mechanisms. It is therefore notable that VSFG bands for the intermediate are not observed with methanol. If they were due to **9** we would have anticipated observing them at the most negative potentials (e.g. -1.65 V_{Ag}) studied where a significant catalytic current does occur due to the reduction first pathway.

Supporting computational results: The energy-favoured orientation of complexes **6** to **8** was screened by considering different initial geometries or equivalently, molecular orientations with respect to the Hg-slab (supplementary figure 14). In each case, the molecular complex was placed to initially have a 3.5 Å shortest distance from the Hg-slab, and eventually allowed to fully relax together with the Hg atoms. Supplementary table 2 reports the computed relative energies. In all cases, geometry **[6]**, for which both the *bpy* and the reacting *COOH/CO* fragments point towards the Hg-surface, results to be energetically favoured. Vibrational analysis was performed only for the energy favoured geometries (**[6]**). Coordinates of the energy favoured orientations of all complexes studied are within the computational raw data files freely available from the University of Liverpool Research Data Catalogue at http://dx.doi.org/10.17638/datacat.liverpool.ac.uk/533

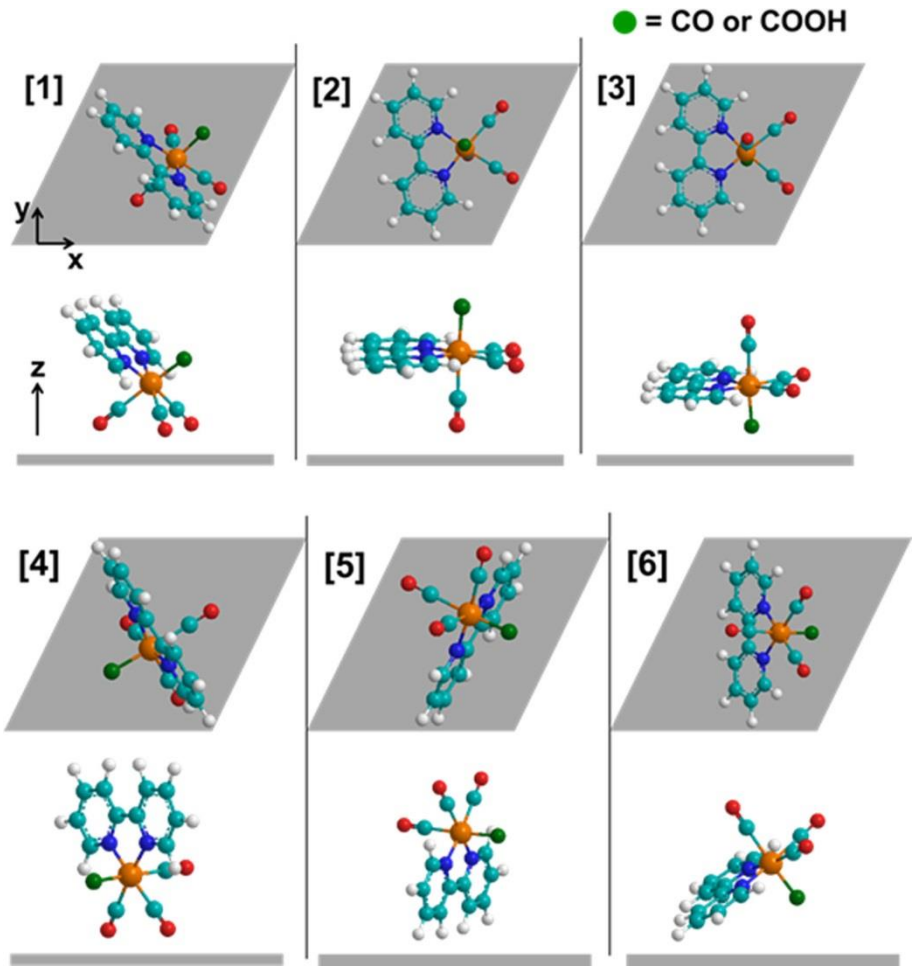

*Supplementary Figure 14: Top (top-panel) and side (bottom-panel) view of the surface geometries studied for complexes **6** to **8**. The labelling used to differentiate geometries is reported in square brackets. Hg(100): silver, H: white, C: cyan, O: red, N: blue, Mn: orange.*

Adsorption geometry	**6**	**7**	**8**
[1]	+0.81	+0.72	+3.39
[2]	+0.80	+0.82	+3.40
[3]	+0.81	+0.71	+3.42
[4]	+0.69	+0.74	+3.36
[5]	+0.81	+0.64	+3.41
[6]	**0.0**	**0.0**	**0.0**

*Supplementary Table 2: Computed relative energies (eV) for the adsorption geometries in supplementary figure 14 of complexes **6** to **8**. Same labelling as in supplementary figure 14.*

Despite the limitations of the adopted semi-local XC-functional (PBE), and expected tendency to over-delocalise excess charge, comparison between the computed Bader charges[7] for the molecular complex (supplementary table 3) indicate that at least 50% (~0.5 e) of the charge added or removed passing from complex **6** to **7** and **8** to **9** remains localised on the molecular system, in qualitative accordance with scheme 1 in the main text.

6	**7**	**8**	**9**
-0.08	-0.58	+1.15	-0.03

*Supplementary Table 3: Computed Bader charges (e) for the complexes **6** to **9** in their energy-favoured adsorption geometry on the Hg(100)-6x6 slab.*

Supplementary figure 15 displays (spin-resolved) analysis of the complex-projected Density of States (PDOS) for the complexes **6** to **9** both *in vacuo* and on the Hg(100)-6x6 slab. In general, interactions with the Hg slab and the ensuing electronic re-hybridisation[8] leads to broadening of the molecular peaks for the complex. Not unexpectedly, such re-hybridisation alters the electronic structure of the complexes with non-negligible effects on the energy position of empty (Kohn-Sham) states with respect to the occupied ones. The computed energy of the LUMO of **6** *in vacuo* is roughly 1 eV lower than for **8**, suggesting that reduction of **6** should be (energetically) favoured over reduction of **8**. However, adsorption of the complexes on Hg(100) leads to inversion of the relative LUMO energies. On Hg(100), the computed LUMO of **6** is roughly 1 eV higher in energy than the LUMO of **8**, suggesting a stronger propensity to reduction for **8**. This result is in qualitative accordance with the observed *protonation-first* (not *reduction-first*) mechanism on Hg-coated electrodes and the past computational studies.[9–11]

The higher energy of the LUMO of **9** with respect to the LUMO of **8** suggests a reduced propensity to reduction of **9** with respect to **8**. However, injection into the system of an additional electron leads to *metallization* (non-zero PDOS at the Fermi energy, E_F) of **9(-)**, where **9(-)** indicates the complex **9** in the presence of an additional electron added to the system (isolated complex and complex-Hg slab), ensuing an increase in the conductivity of the **9(-)**/Hg(100) interface, as experimentally observed for reduction at an applied potential negative of -1.25 V (figure 1). Based on the computed metallization of the adsorbed complex, indicative of strongly enhanced electronic coupling with the underlying Hg substrate (thence electronic conductance, see figure 1), reduction of **9(-)** is expected to proceed substantially faster than for **8**.

Overall, simulation of the complexes **6** to **9(-)** demonstrate that interfacial electronic re-hybridization is sensitive to both the chemical composition of the catalyst and the amount of extra charge present at the electrode surface (due to the applied bias). As evident from supplementary figure 15, different reaction intermediates can interact differently with a differently charged surface, resulting in variable electronic coupling with the underlying substrate. This aspect could be further developed in the quest of enhanced electro-catalysts. Tuneable metallization of molecular catalysts and intermediates may offer alternatives to permanent metallization (strong electronic coupling) of the catalyst by covalent bonding to the electrode in the quest of strategies to conveniently alter reaction energy profiles, thence control reaction kinetics and mechanisms.[12,13]

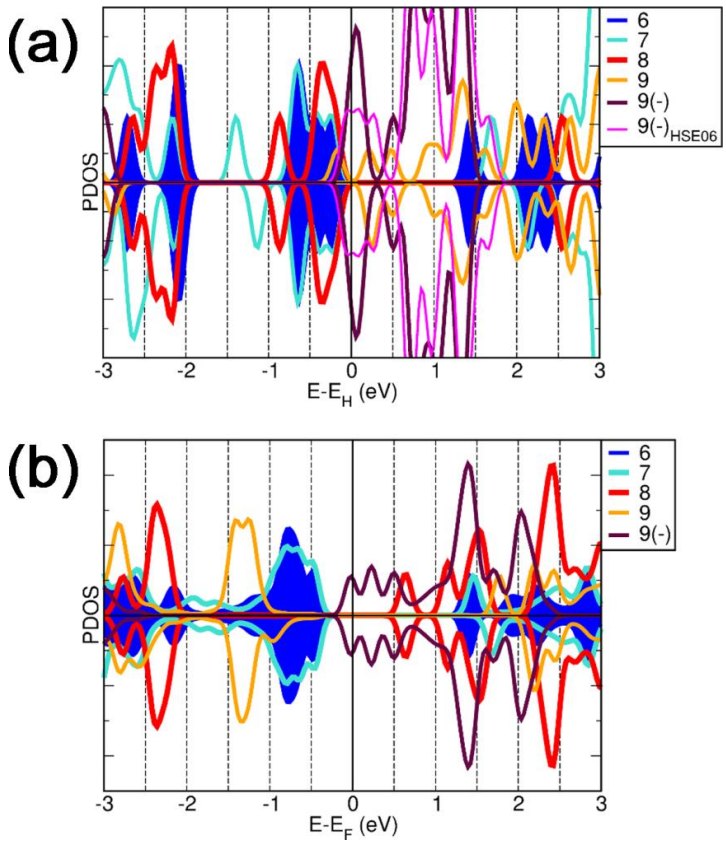

*Supplementary Figure 15: Spin-resolved, complex-projected Density of States (PDOS) for the complexes **6** to **9** in vacuo (a) and on the Hg(100)-6x6 slab (b). The horizontal energy axis has been scaled to the computed energy of the HOMO for the complex (E_H) in (a) and Fermi energy (E_F) of the composite complex-Hg slab system in (b). **9(-)** indicates the complex **9** in the presence of an additional electron added to the system (isolated complex and complex-Hg slab). All the PDOS traces have been smeared by mean of 0.1 eV Full-width at half maximum gaussian functions centered on the computed (Kohn-Sham) eigenvalues. Additional hybrid DFT HSE06[14] single-point calculation (on the PBE-optimized geometry) for the isolated complex **9(-)** (magenta trace) qualitatively confirm the PBE result (brown trace) of re-hybridisation of the lowest energy empty Kohn-Sham states of **9** (orange trace) following electron addition.*

System	$\hat{\nu}_1$	$\hat{\nu}_2$	$\hat{\nu}_3$	$\hat{\nu}_4$	$\hat{\nu}_{bpy}$
1_v (CH_3CN)	2049.18	1992.11	1978.99	N.A.	1598.73
1_v (Br)	2014.40	1951.44	1940.03	N.A.	1597.30
1_{exp} (Br)					**1604**
6_v	2008.84	1943.77	1940.99	**1657.81**	1596.80
6^*_v	2009.76 (-0.92)	1943.98 (-0.21)	1941.65 (-0.66)	**1582.88 (-74.93)**	1597.97 (-1.17)
6_{Hg}	2007.36	1945.79	1940.03	**1598.56**	1592.23
6^*_{Hg}	2007.27 (-0.09)	1945.36 (-0.43)	1939.77 (-0.26)	**1527.04 (-71.52)**	1593.40 (-1.17)
7_v	1977.66	1899.47	1895.46	**1637.06**	1569.06
7^*_v	1977.15 (-0.51)	1899.08 (-0.39)	1894.22 (-1.24)	**1566.02 (-71.04)**	1569.09 (+0.03)
7_{Hg}	1987.72	1920.00	1915.69	**1596.24**	1564.95
7^*_{Hg}	1987.85 (+0.13)	1920.66 (+0.66)	1915.22 (-0.47)	**1530.31 (-65.93)**	1564.55 (-0.40)
8_v	**2105.78**	**2034.08**	**2029.46**	**2004.99**	1598.77
8^*_v	**2087.50 (-18.28)**	**2029.80 (-4.28)**	**2004.93 (-24.53)**	**1955.19 (-49.80)**	1598.53 (-0.24)
8_{exp}	**2118**	**2044**	**2023**	**1982**	
8_{Hg}	**2099.90**	**2025.66**	**2020.91**	**1996.45**	1593.92
8^*_{Hg} (down)	**2082.81 (-17.09)**	**2024.10 (-1.56)**	**1996.84 (-24.07)**	**1943.73 (-52.72)**	1593.47 (-0.45)
8^*_{Hg} (up)	**2080.26 (-19.64)**	**2020.80 (-4.86)**	**1997.04 (-23.87)**	**1949.27 (-47.18)**	1594.28 (+0.36)
9_v	**2074.31**	**2002.24**	**1992.19**	**1962.20**	1564.93
9^*_v	**2056.25 (-18.06)**	**1993.41 (-8.83)**	**1961.65 (-30.54)**	**1924.97 (-37.23)**	1564.57 (-0.36)
9_{Hg}	**2071.25**	**1997.23**	**1988.94**	**1964.37**	1558.88
9^*_{Hg} (down)	**2055.41 (-15.84)**	**1994.78 (-2.45)**	**1963.74 (-25.20)**	**1912.71 (-51.66)**	1558.35 (-0.53)
9^*_{Hg} (up)	**2049.87 (-21.38)**	**1989.37 (-7.86)**	**1963.79 (-25.15)**	**1923.84 (-40.53)**	1558.94 (+0.06)

*Supplementary Table 4: Summary of computed wavenumbers (cm^{-1}) for CO (COOH) and highest-energy bpy modes of pristine and isotopically labelled (*) complexes **1** and **6** to **9** in vacuo (v) and on the Hg model surface (Hg). Computed values are the same as in Fig. 7 and supplementary tables 5-22. Where available, experimental values (exp, **8** reference [4], **1**-Br ($Mn(bpy)(CO)_3Br$) this work) for the complex in solution are also provided. For isotopically labelled systems, the induced shift with respect to the pristine system is reported in brackets.*

Supplementary table 4 summarises all of the calculated IR modes discussed in the main text and included in the data tables below. Here we highlight key points of these calculations that build upon the discussion in the main text.

- Our calculations demonstrate that isotopic labelling of **6** and **7** is not able to reproduce the observed shift in the VSFG region in the 2000-1900 cm^{-1} experimentally determined in the main text (figure 5). In contrast when both at the surface or in vacuo complexes **8** and **9** are able to.
- The highest energy bpy modes are calculated to be largely insensitive to the presence of the Hg surface and the calculated wavenumber for **1** both in vacuo and on Hg matches the experimentally determined value in solution. Experimentally we observe the bpy modes show minimal dependence on the applied potential (changing electric field) therefore the calculated values of the highest energy bpy modes of **8** and **9** on Hg are believed to provide a suitable method to discriminate between these two complexes.
- In contrast, as evident from the VSFG spectra recorded during CV's (figure 4), the ν(CO) peak of the intermediate at 1976 cm^{-1} shows a rather clear Stark shift (~17 cm^{-1} V^{-1} slope) as the applied potential is changed from more negative (-1.60 V) to less negative (-1.35 V), which reduces the polarisation of electrode and of the electric field across the double-layer containing the intermediate. One is thus to conclude that reduction of the electric field across the double-layer for the reaction intermediate hardens the modes under the VSFG-detected peak in figure 4. We have investigated this aspect by computing the vibrational modes of **8** and **9** in the presence of an external electric-field. For this analysis, we re-optimised **8** and **9** in vacuo but with the same orientation as the energy favoured adsorption geometry on the Hg-surface (figure 7). For the sign convention used, more negative electric field correspond to accumulation of more negative charge under the tripod formed by the Mn-bpy and Mn-CO_d bonds (figure 8). As shown in figure 8 (main text), only complex **8** is found to have one specific CO mode that significantly hardens upon reduction of the intensity of the external electric field. All other modes of **8** (and all the modes of **9**) either do not significantly respond to the external field or show changes incompatible with the experimentally measured field-induced softening of the vibration (Stark shift in figure 4).
- Notably, the only mode of **8** compatible with the observed Stark shift in the VSFG peak is characterised by field-dependent contributions from the both the axial (CO_d) and equatorial (CO_{eq}) CO ligands. As shown in figure 8 (main text) the simulations indicate the contribution from CO_d becomes larger (and CO_{eq} becomes smaller) as the intensity of the external electric field grows. This result is compatible with the measured isotopic shift observed upon labelling of the axial CO.

$\hat{\nu}$ (cm^{-1})	CO_{eq}	CO_{ax}	COOH	bpy
2008.84	**0.698**	**0.297**	0.002	0.001
1943.77	**0.541**	**0.457**	0.000	0.000
1940.99	**0.755**	**0.243**	0.000	0.000
1657.81	0.002	0.000	**0.991**	0.006
1596.80	0.000	0.000	0.003	**0.996**
1595.07	0.000	0.000	0.000	**0.999**
1560.72	0.000	0.000	0.000	**0.999**
1548.88	0.000	0.000	0.000	**0.999**
1473.25	0.000	0.000	0.001	**0.997**
1456.34	0.000	0.000	0.000	**0.999**
1433.42	0.000	0.000	0.000	**0.999**
1416.94	0.000	0.000	0.000	**0.999**
1319.76	0.000	0.000	0.000	**0.999**
1313.55	0.000	0.000	0.000	**0.999**
1311.50	0.000	0.000	0.000	**0.999**
1289.05	0.000	0.000	0.000	**0.998**
1271.46	0.000	0.000	0.003	**0.995**
1222.97	0.000	0.000	**0.994**	0.005
1159.52	0.000	0.000	0.000	**0.999**
1141.94	0.000	0.000	0.000	**0.999**
1115.04	0.000	0.000	0.000	**0.999**
1102.09	0.000	0.000	0.000	**0.998**

*Supplementary Table 5: Fragment-resolved contribution (P_a) to the vibrational modes of the isolated complex **6** in the 2,200-1,100 cm^{-1} range.*

$\hat{\nu}$ (cm^{-1})	CO_{eq}	CO_{ax}	COOH	bpy
2009.76	**0.708**	**0.288**	0.001	0.001
1943.98	**0.654**	**0.345**	0.000	0.000
1941.65	**0.633**	**0.365**	0.000	0.000
1597.97	0.000	0.000	0.057	**0.941**
1594.30	0.000	0.000	0.001	**0.998**
1582.88	0.001	0.000	**0.930**	**0.068**
1559.68	0.000	0.000	0.001	**0.998**
1547.88	0.000	0.000	0.002	**0.997**
1472.91	0.000	0.000	0.003	**0.995**
1456.53	0.000	0.000	0.000	**0.999**
1432.90	0.000	0.000	0.000	**0.999**
1416.44	0.000	0.000	0.000	**0.999**
1320.51	0.000	0.000	0.000	**0.999**
1313.24	0.000	0.000	0.000	**0.999**
1311.31	0.000	0.000	0.000	**0.999**
1290.03	0.000	0.000	0.000	**0.998**
1271.78	0.000	0.000	0.001	**0.997**
1204.87	0.000	0.000	**0.997**	0.002
1161.46	0.000	0.000	0.000	**0.999**
1144.97	0.000	0.000	0.000	**0.999**
1118.55	0.000	0.000	0.000	**0.999**
1104.31	0.000	0.000	0.000	**0.998**

*Supplementary Table 6: Fragment-resolved contribution (P_a) to the vibrational modes of the isolated isotopically labelled complex **6** (**6***) in the 2,200-1,100 cm^{-1} range.*

$\hat{\nu}$ (cm^{-1})	CO_{eq}	CO_{ax}	COOH	bpy
1977.66	**0.663**	**0.331**	0.003	0.000
1899.47	**0.404**	**0.594**	0.000	0.000
1895.46	**0.926**	0.072	0.000	0.000
1637.06	0.002	0.000	**0.995**	0.001
1569.06	0.000	0.000	0.000	**0.999**
1563.68	0.000	0.000	0.000	**0.999**
1503.14	0.000	0.000	0.000	**0.999**
1472.50	0.000	0.000	0.000	**0.999**
1471.75	0.000	0.000	0.000	**0.999**
1450.31	0.000	0.000	0.000	**0.999**
1412.09	0.000	0.000	0.000	**0.999**
1408.11	0.000	0.000	0.000	**0.999**
1348.19	0.000	0.000	0.000	**0.999**
1326.81	0.000	0.000	0.000	**0.999**
1318.06	0.000	0.000	0.000	**0.999**
1278.52	0.000	0.000	0.000	**0.999**
1213.21	0.000	0.000	0.090	**0.909**
1211.68	0.000	0.000	**0.908**	**0.091**
1141.13	0.000	0.000	0.000	**0.999**
1124.87	0.000	0.000	0.000	**0.999**
1102.04	0.000	0.000	0.000	**0.999**

*Supplementary Table 7: Fragment-resolved contribution (P_a) to the vibrational modes of the isolated complex **7** in the 2,200-1,100 cm^{-1} range.*

$\hat{\nu}$ (cm^{-1})	CO_{eq}	CO_{ax}	COOH	bpy
1977.15	**0.663**	**0.332**	0.002	0.000
1899.08	**0.435**	**0.563**	0.000	0.000
1894.22	**0.896**	**0.102**	0.000	0.000
1569.09	0.000	0.000	**0.027**	**0.972**
1566.02	0.001	0.000	**0.703**	**0.294**
1562.73	0.000	0.000	**0.264**	**0.734**
1503.24	0.000	0.000	0.000	**0.999**
1471.71	0.000	0.000	0.000	**0.999**
1470.89	0.000	0.000	0.001	**0.998**
1450.35	0.000	0.000	0.000	**0.999**
1412.11	0.000	0.000	0.000	**0.999**
1407.42	0.000	0.000	0.000	**0.999**
1348.28	0.000	0.000	0.000	**0.999**
1326.56	0.000	0.000	0.000	**0.999**
1317.12	0.000	0.000	0.000	**0.999**
1279.17	0.000	0.000	0.000	**0.999**
1213.32	0.000	0.000	0.000	**0.999**
1190.02	0.000	0.000	**0.998**	0.001
1143.64	0.000	0.000	0.000	**0.999**
1125.38	0.000	0.000	0.000	**0.999**
1107.10	0.000	0.000	0.000	**0.999**

*Supplementary Table 8: Fragment-resolved contribution (P_a) to the vibrational modes of the isolated, isotopically labelled complex **7** (**7***) in the 2,200-1,100 cm^{-1} range.*

$\hat{\nu}$ (cm^{-1})	CO_{eq}	CO_{ax}	CO_{d}	bpy
2105.78	**0.236**	**0.378**	**0.383**	0.000
2034.08	0.003	**0.469**	**0.526**	0.000
2029.46	**0.759**	**0.151**	**0.089**	0.000
2004.99	**0.999**	0.000	0.000	0.000
1598.77	0.000	0.000	0.000	**0.999**
1594.36	0.000	0.000	0.000	**0.999**
1566.59	0.000	0.000	0.000	**0.999**
1557.88	0.000	0.000	0.000	**0.999**
1486.18	0.000	0.000	0.000	**0.999**
1460.44	0.000	0.000	0.000	**0.999**
1435.37	0.000	0.000	0.000	**0.999**
1420.42	0.000	0.000	0.000	**0.999**
1325.16	0.000	0.000	0.000	**0.999**
1313.46	0.000	0.000	0.000	**0.999**
1311.10	0.000	0.000	0.000	**0.999**
1290.88	0.000	0.000	0.000	**0.999**
1278.50	0.000	0.000	0.000	**0.999**
1172.64	0.000	0.000	0.000	**0.999**
1154.62	0.000	0.000	0.000	**0.999**
1124.33	0.000	0.000	0.000	**0.999**
1108.84	0.000	0.000	0.000	**0.999**

*Supplementary Table 9: Fragment-resolved contribution (P_a) to the vibrational modes of the isolated complex **8** in the 2,200-1,100 cm^{-1} range.*

$\hat{\nu}$ (cm^{-1})	CO_{eq}	CO_{ax}	CO_{d}	bpy
2087.50	**0.346**	**0.579**	**0.074**	0.000
2029.80	**0.621**	**0.378**	0.000	0.000
2004.93	**0.999**	0.000	0.000	0.000
1955.19	**0.032**	**0.042**	**0.925**	0.000
1598.53	0.000	0.000	0.000	**0.999**
1594.64	0.000	0.000	0.000	**0.999**
1567.37	0.000	0.000	0.000	**0.999**
1558.32	0.000	0.000	0.000	**0.999**
1486.42	0.000	0.000	0.000	**0.999**
1460.99	0.000	0.000	0.000	**0.999**
1436.94	0.000	0.000	0.000	**0.999**
1420.20	0.000	0.000	0.000	**0.999**
1326.45	0.000	0.000	0.000	**0.999**
1313.21	0.000	0.000	0.000	**0.999**
1311.02	0.000	0.000	0.000	**0.999**
1291.25	0.000	0.000	0.000	**0.999**
1279.13	0.000	0.000	0.000	**0.999**
1173.68	0.000	0.000	0.000	**0.999**
1156.05	0.000	0.000	0.000	**0.999**
1122.84	0.000	0.000	0.000	**0.999**
1110.30	0.000	0.000	0.000	**0.999**

*Supplementary Table 10: Fragment-resolved contribution (P_a) to the vibrational modes of the isolated, isotopically labelled complex **8** (**8* down**) in the 2,200-1,100 cm^{-1} range.*

$\hat{\nu}$ (cm^{-1})	CO_{eq}	CO_{ax}	CO_{d}	bpy
2074.31	**0.210**	**0.396**	**0.392**	0.000
2002.24	0.000	**0.490**	**0.508**	0.000
1992.19	**0.788**	**0.112**	**0.098**	0.000
1962.20	**0.999**	0.000	0.000	0.000
1564.93	0.000	0.000	0.000	**0.999**
1547.21	0.000	0.000	0.000	**0.999**
1502.15	0.000	0.000	0.000	**0.999**
1497.28	0.000	0.000	0.000	**0.999**
1490.95	0.000	0.000	0.000	**0.999**
1450.67	0.000	0.000	0.000	**0.999**
1418.65	0.000	0.000	0.000	**0.999**
1414.12	0.000	0.000	0.000	**0.999**
1353.50	0.000	0.000	0.000	**0.999**
1321.93	0.000	0.000	0.000	**0.999**
1311.97	0.000	0.000	0.000	**0.999**
1279.30	0.000	0.000	0.000	**0.999**
1214.60	0.000	0.000	0.000	**0.999**
1152.84	0.000	0.000	0.000	**0.999**
1134.57	0.000	0.000	0.000	**0.999**
1115.33	0.000	0.000	0.000	**0.999**

*Supplementary Table 11: Fragment-resolved contribution (P_a) to the vibrational modes of the isolated complex **9** in the 2,200-1,100 cm^{-1} range.*

$\hat{\nu}$ (cm^{-1})	CO_{eq}	CO_{ax}	CO_{d}	bpy
2056.25	**0.290**	**0.629**	**0.079**	0.000
1993.41	**0.666**	**0.329**	0.003	0.000
1961.65	**0.999**	0.000	0.000	0.000
1924.97	**0.042**	**0.039**	**0.917**	0.000
1564.57	0.000	0.000	0.000	**0.999**
1547.38	0.000	0.000	0.000	**0.999**
1502.53	0.000	0.000	0.000	**0.999**
1496.92	0.000	0.000	0.000	**0.999**
1490.34	0.000	0.000	0.000	**0.999**
1450.64	0.000	0.000	0.000	**0.999**
1418.50	0.000	0.000	0.000	**0.999**
1412.57	0.000	0.000	0.000	**0.999**
1353.04	0.000	0.000	0.000	**0.999**
1321.09	0.000	0.000	0.000	**0.999**
1311.39	0.000	0.000	0.000	**0.999**
1280.92	0.000	0.000	0.000	**0.999**
1214.94	0.000	0.000	0.000	**0.999**
1153.21	0.000	0.000	0.000	**0.999**
1136.51	0.000	0.000	0.000	**0.999**
1120.07	0.000	0.000	0.000	**0.999**

*Supplementary Table 12: Fragment-resolved contribution (P_a) to the vibrational modes of the isolated, isotopically labelled complex **9** (**9* down**) in the 2,200-1,100 cm^{-1} range.*

$\hat{\nu}$ (cm^{-1})	CO_{eq}	CO_{ax}	COOH	bpy
2007.36	**0.647**	**0.349**	0.001	0.001
1945.79	**0.351**	**0.648**	0.000	0.000
1940.03	**0.998**	0.000	0.000	0.000
1598.56	0.001	0.001	**0.744**	**0.252**
1592.23	0.000	0.000	0.000	**0.999**
1589.86	0.000	0.000	**0.247**	**0.752**
1558.06	0.000	0.000	0.000	**0.999**
1546.52	0.000	0.000	0.000	**0.999**
1475.71	0.000	0.000	0.003	**0.996**
1453.65	0.000	0.000	0.000	**0.999**
1429.16	0.000	0.000	0.000	**0.999**
1414.45	0.000	0.000	0.001	**0.998**
1321.10	0.000	0.000	0.000	**0.998**
1312.00	0.000	0.000	0.000	**0.999**
1311.65	0.000	0.000	0.000	**0.999**
1289.23	0.000	0.000	0.000	**0.999**
1271.72	0.000	0.000	0.003	**0.996**
1244.43	0.000	0.000	**0.995**	0.004
1160.16	0.000	0.000	0.000	**0.999**
1141.31	0.000	0.000	0.000	**0.999**
1116.20	0.000	0.000	0.000	**0.999**
1103.12	0.000	0.000	0.001	**0.998**

*Supplementary Table 13: Fragment-resolved contribution (P_a) to the vibrational modes of complex **6** in the 2,200-1,100 cm^{-1} range at the Hg surface.*

$\hat{\nu}$ (cm^{-1})	CO_{eq}	CO_{ax}	COOH	bpy
2007.27	**0.650**	**0.346**	0.001	0.001
1945.36	**0.349**	**0.650**	0.000	0.000
1939.77	**0.997**	0.001	0.000	0.000
1593.40	0.000	0.000	0.000	**0.998**
1591.92	0.000	0.000	0.001	**0.997**
1558.42	0.000	0.000	0.000	**0.999**
1546.55	0.000	0.000	0.002	**0.997**
1527.04	0.000	0.000	**0.976**	0.022
1475.27	0.000	0.000	0.013	**0.985**
1453.90	0.000	0.000	0.000	**0.999**
1428.65	0.000	0.000	0.000	**0.999**
1414.15	0.000	0.000	0.002	**0.997**
1319.64	0.000	0.000	0.000	**0.999**
1312.82	0.000	0.000	0.000	**0.999**
1311.11	0.000	0.000	0.000	**0.999**
1288.54	0.000	0.000	0.000	**0.999**
1270.45	0.000	0.000	0.000	**0.998**
1224.85	0.000	0.000	**0.998**	0.001
1160.61	0.000	0.000	0.000	**0.999**
1140.78	0.000	0.000	0.000	**0.999**
1117.09	0.000	0.000	0.000	**0.999**
1102.67	0.000	0.000	0.000	**0.999**

*Supplementary Table 14: Fragment-resolved contribution (P_a) to the vibrational modes of the isotopically labelled complex **6** (**6***) in the 2,200-1,100 cm^{-1} range at the Hg surface.*

$\hat{\nu}$ (cm^{-1})	CO_{eq}	CO_{ax}	COOH	bpy
1987.72	**0.646**	**0.350**	0.001	0.000
1920.00	**0.359**	**0.640**	0.000	0.000
1915.69	**0.991**	0.007	0.000	0.000
1596.24	0.000	0.001	**0.993**	0.004
1564.95	0.000	0.000	0.000	**0.999**
1526.04	0.000	0.000	0.003	**0.996**
1512.13	0.000	0.000	0.000	**0.999**
1504.89	0.000	0.000	0.000	**0.999**
1452.03	0.000	0.000	0.000	**0.999**
1449.43	0.000	0.000	0.000	**0.999**
1417.87	0.000	0.000	0.000	**0.999**
1406.56	0.000	0.000	0.000	**0.999**
1331.26	0.000	0.000	0.000	**0.999**
1315.72	0.000	0.000	0.000	**0.999**
1310.78	0.000	0.000	0.000	**0.999**
1287.17	0.000	0.000	0.000	**0.999**
1235.84	0.000	0.000	**0.699**	**0.300**
1234.03	0.000	0.000	**0.300**	**0.699**
1150.40	0.000	0.000	0.000	**0.999**
1132.23	0.000	0.000	0.000	**0.999**
1111.08	0.000	0.000	0.000	**0.999**

*Supplementary Table 15: Fragment-resolved contribution (P_a) to the vibrational modes of complex **7** in the 2,200-1,100 cm^{-1} range at the Hg surface.*

$\hat{\nu}$ (cm^{-1})	CO_{eq}	CO_{ax}	COOH	bpy
1987.85	**0.639**	**0.357**	0.001	0.000
1920.66	**0.363**	**0.636**	0.000	0.000
1915.22	**0.994**	0.004	0.000	0.000
1564.55	0.000	0.000	0.000	**0.999**
1530.31	0.000	0.000	**0.443**	**0.555**
1522.24	0.000	0.000	**0.551**	**0.447**
1512.02	0.000	0.000	0.000	**0.999**
1504.74	0.000	0.000	0.000	**0.998**
1452.23	0.000	0.000	0.000	**0.998**
1449.36	0.000	0.000	0.000	**0.999**
1417.73	0.000	0.000	0.000	**0.999**
1406.58	0.000	0.000	0.001	**0.998**
1330.61	0.000	0.000	0.000	**0.999**
1315.78	0.000	0.000	0.000	**0.999**
1310.39	0.000	0.000	0.000	**0.999**
1287.25	0.000	0.000	0.000	**0.999**
1235.00	0.000	0.000	0.000	**0.999**
1215.10	0.000	0.000	**0.998**	0.000
1151.42	0.000	0.000	0.000	**0.999**
1132.38	0.000	0.000	0.000	**0.999**
1111.09	0.000	0.000	0.000	**0.999**

*Supplementary Table 16: Fragment-resolved contribution (P_a) to the vibrational modes of the isotopically labelled complex **7** (**7***) in the 2,200-1,100 cm^{-1} range at the Hg surface.*

$\hat{\nu}$ (cm^{-1})	CO_{eq}	CO_{ax}	CO_{d}	bpy
2099.90	**0.234**	**0.407**	**0.357**	0.000
2025.66	**0.160**	**0.592**	**0.246**	0.000
2020.91	**0.603**	0.000	**0.395**	0.000
1996.45	**0.999**	0.000	0.000	0.000
1593.92	0.000	0.000	0.000	**0.999**
1586.72	0.000	0.000	0.000	**0.999**
1561.65	0.000	0.000	0.000	**0.999**
1553.60	0.000	0.000	0.000	**0.999**
1486.81	0.000	0.000	0.000	**0.999**
1458.36	0.000	0.000	0.000	**0.999**
1433.99	0.000	0.000	0.000	**0.999**
1417.98	0.000	0.000	0.000	**0.999**
1326.18	0.000	0.000	0.000	**0.999**
1313.13	0.000	0.000	0.000	**0.999**
1310.14	0.000	0.000	0.000	**0.999**
1293.48	0.000	0.000	0.000	**0.999**
1277.04	0.000	0.000	0.000	**0.999**
1169.00	0.000	0.000	0.000	**0.999**
1149.39	0.000	0.000	0.000	**0.999**
1119.37	0.000	0.000	0.000	**0.999**
1106.45	0.000	0.000	0.000	**0.999**

*Supplementary Table 17: Fragment-resolved contribution (P_a) to the vibrational modes of complex **8** in the 2,200-1,100 cm^{-1} range at the Hg surface.*

$\hat{\nu}$ (cm^{-1})	CO_{eq}	CO_{ax}	CO_{d}	bpy
2082.81	**0.325**	**0.599**	0.074	0.000
2024.10	**0.640**	**0.358**	0.000	0.000
1996.84	**0.999**	0.000	0.000	0.000
1943.73	0.033	0.041	**0.924**	0.000
1593.47	0.000	0.000	0.000	**0.999**
1586.71	0.000	0.000	0.000	**0.999**
1561.88	0.000	0.000	0.000	**0.999**
1553.64	0.000	0.000	0.000	**0.999**
1486.69	0.000	0.000	0.000	**0.999**
1457.88	0.000	0.000	0.000	**0.999**
1433.52	0.000	0.000	0.000	**0.999**
1418.00	0.000	0.000	0.000	**0.999**
1326.76	0.000	0.000	0.000	**0.999**
1313.15	0.000	0.000	0.000	**0.999**
1309.69	0.000	0.000	0.000	**0.999**
1293.72	0.000	0.000	0.000	**0.999**
1278.20	0.000	0.000	0.000	**0.999**
1168.01	0.000	0.000	0.000	**0.999**
1150.08	0.000	0.000	0.000	**0.999**
1120.00	0.000	0.000	0.000	**0.999**
1106.45	0.000	0.000	0.000	**0.999**

*Supplementary Table 18: Fragment-resolved contribution (P_a) to the vibrational modes of the isotopically labelled complex **8** (**8* down**) in the 2,200-1,100 cm^{-1} range at the Hg surface.*

$\hat{\nu}$ (cm^{-1})	CO_{eq}	CO_{ax}	CO_{u}	bpy
2080.26	**0.372**	**0.543**	0.084	0.000
2020.80	**0.595**	**0.404**	0.000	0.000
1997.04	**0.999**	0.000	0.000	0.000
1949.27	0.031	0.052	**0.915**	0.000
1594.28	0.000	0.000	0.000	**0.999**
1587.18	0.000	0.000	0.000	**0.999**
1561.33	0.000	0.000	0.000	**0.999**
1553.52	0.000	0.000	0.000	**0.999**
1486.89	0.000	0.000	0.000	**0.999**
1458.52	0.000	0.000	0.000	**0.999**
1433.86	0.000	0.000	0.000	**0.999**
1418.23	0.000	0.000	0.000	**0.999**
1326.54	0.000	0.000	0.000	**0.999**
1312.93	0.000	0.000	0.000	**0.999**
1310.43	0.000	0.000	0.000	**0.999**
1293.68	0.000	0.000	0.000	**0.999**
1278.42	0.000	0.000	0.000	**0.999**
1168.14	0.000	0.000	0.000	**0.999**
1149.67	0.000	0.000	0.000	**0.999**
1119.70	0.000	0.000	0.000	**0.999**
1106.18	0.000	0.000	0.000	**0.999**

*Supplementary Table 19: Fragment-resolved contribution (P_a) to the vibrational modes of the isotopically labelled complex **8** (**8* up**) in the 2,200-1,100 cm^{-1} range at the Hg surface.*

$\hat{\nu}$ (cm^{-1})	CO_{eq}	CO_{ax}	CO_{d}	bpy
2071.25	**0.234**	**0.445**	**0.318**	0.000
1997.23	**0.258**	**0.548**	**0.192**	0.000
1988.94	**0.505**	0.005	**0.488**	0.000
1964.37	**0.998**	0.000	0.000	0.000
1558.88	0.000	0.000	0.000	**0.999**
1534.41	0.000	0.000	0.000	**0.999**
1499.26	0.000	0.000	0.000	**0.999**
1497.08	0.000	0.000	0.000	**0.999**
1487.98	0.000	0.000	0.000	**0.999**
1448.53	0.000	0.000	0.000	**0.999**
1415.57	0.000	0.000	0.000	**0.999**
1412.85	0.000	0.000	0.000	**0.999**
1350.01	0.000	0.000	0.000	**0.999**
1318.49	0.000	0.000	0.000	**0.999**
1308.22	0.000	0.000	0.000	**0.999**
1279.95	0.000	0.000	0.000	**0.999**
1215.18	0.000	0.000	0.000	**0.999**
1154.30	0.000	0.000	0.000	**0.999**
1135.40	0.000	0.000	0.000	**0.999**
1117.26	0.000	0.000	0.000	**0.999**

*Supplementary Table 20: Fragment-resolved contribution (P_a) to the vibrational modes of complex **9** in the 2,200-1,100 cm^{-1} range at the Hg surface.*

$\hat{\nu}$ (cm^{-1})	CO_{eq}	CO_{ax}	CO_{d}	bpy
2055.41	**0.301**	**0.626**	0.071	0.000
1994.78	**0.661**	**0.335**	0.001	0.000
1963.74	**0.999**	0.000	0.000	0.000
1912.71	0.035	0.037	**0.926**	0.000
1558.35	0.000	0.000	0.000	**0.999**
1533.90	0.000	0.000	0.000	**0.999**
1499.57	0.000	0.000	0.000	**0.999**
1497.16	0.000	0.000	0.000	**0.999**
1488.10	0.000	0.000	0.000	**0.999**
1448.19	0.000	0.000	0.000	**0.999**
1415.88	0.000	0.000	0.000	**0.999**
1412.28	0.000	0.000	0.000	**0.999**
1350.26	0.000	0.000	0.000	**0.999**
1320.07	0.000	0.000	0.000	**0.999**
1309.01	0.000	0.000	0.000	**0.999**
1280.33	0.000	0.000	0.000	**0.999**
1216.81	0.000	0.000	0.000	**0.999**
1153.38	0.000	0.000	0.000	**0.999**
1137.64	0.000	0.000	0.000	**0.999**
1118.13	0.000	0.000	0.000	**0.999**

*Supplementary Table 21. Fragment-resolved contribution (P_a) to the vibrational modes of the isotopically labelled complex **9** (**9* down**) in the 2,200-1,100 cm^{-1} range at the Hg surface.*

$\hat{\nu}$ (cm^{-1})	CO_{eq}	CO_{ax}	CO_u	bpy
2049.87	**0.376**	**0.531**	0.091	0.000
1989.37	**0.587**	**0.411**	0.000	0.000
1963.79	**0.999**	0.000	0.000	0.000
1923.84	0.035	0.056	**0.907**	0.000
1558.94	0.000	0.000	0.000	**0.999**
1535.36	0.000	0.000	0.000	**0.999**
1499.34	0.000	0.000	0.000	**0.999**
1497.19	0.000	0.000	0.000	**0.999**
1488.81	0.000	0.000	0.000	**0.999**
1448.40	0.000	0.000	0.000	**0.999**
1416.06	0.000	0.000	0.000	**0.999**
1413.49	0.000	0.000	0.000	**0.999**
1349.72	0.000	0.000	0.000	**0.999**
1320.20	0.000	0.000	0.000	**0.999**
1308.85	0.000	0.000	0.000	**0.999**
1279.78	0.000	0.000	0.000	**0.999**
1215.83	0.000	0.000	0.000	**0.999**
1152.69	0.000	0.000	0.000	**0.999**
1132.44	0.000	0.000	0.000	**0.999**
1118.37	0.000	0.000	0.000	**0.999**

*Supplementary Table 22: Fragment-resolved contribution (P_a) to the vibrational modes of the isotopically labelled complex **9** (**9* up**) in the 2,200-1,100 cm^{-1} range at the Hg surface.*

Supplementary References

1. Walsh, J. J., Neri, G., Smith, C. L. & Cowan, A. J. Electrocatalytic CO2 reduction with a membrane supported manganese catalyst in aqueous solution. *Chem. Commun.* **50,** 12698–12701 (2014).
2. Grills, D. C. *et al.* Mechanism of the Formation of a Mn-Based CO2 Reduction Catalyst Revealed by Pulse Radiolysis with Time-Resolved Infrared Detection. *J. Am. Chem. Soc.* **136,** 5563–5566 (2014).
3. Franco, F. *et al.* Local Proton Source in Electrocatalytic CO_2 Reduction with [Mn(bpy-R)$(CO)_3$Br] Complexes. *Chem. - A Eur. J.* **23,** 4782–4793 (2017).
4. Scheiring, T., Kaim, W. & Fiedler, J. Geometrical and electronic structures of the acetyl complex Re(bpy)(CO)3(COCH3) and of [M(bpy)(CO)4](OTf), M=Mn,Re. *J. Organomet. Chem.* **598,** 136–141 (2000).
5. Bard, A. J. & Faulkner, L. R. *Electrochemical Methods: Fundamentals and Applications, 2nd Edition*. (Wiley, 2001).
6. Rey, N. G. & Dlott, D. D. Studies of electrochemical interfaces by broadband sum frequency

generation. *J. Electroanal. Chem.* **800,** 114–125 (2017).

7. Henkelman, G., Arnaldsson, A. & Jónsson, H. A fast and robust algorithm for Bader decomposition of charge density. *Comput. Mater. Sci.* **36,** 354–360 (2006).

8. Sanvito, S. Molecular spintronics: The rise of spinterface science. *Nat. Phys.* **6,** 562–564 (2010).

9. Riplinger, C., Sampson, M. D., Ritzmann, A. M., Kubiak, C. P. & Carter, E. A. Mechanistic Contrasts between Manganese and Rhenium Bipyridine Electrocatalysts for the Reduction of Carbon Dioxide. *J. Am. Chem. Soc.* **136,** 16285–16298 (2014).

10. Riplinger, C. & Carter, E. A. Influence of Weak Brønsted Acids on Electrocatalytic CO_2 Reduction by Manganese and Rhenium Bipyridine Catalysts. *ACS Catal.* **5,** 900–908 (2015).

11. Lam, Y. C., Nielsen, R. J., Gray, H. B. & Goddard, W. A. A Mn Bipyrimidine Catalyst Predicted To Reduce CO_2 at Lower Overpotential. *ACS Catal.* **5,** 2521–2528 (2015).

12. Oh, S., Gallagher, J. R., Miller, J. T. & Surendranath, Y. Graphite-Conjugated Rhenium Catalysts for Carbon Dioxide Reduction. *J. Am. Chem. Soc.* **138,** 1820–1823 (2016).

13. Fukushima, T., Drisdell, W., Yano, J. & Surendranath, Y. Graphite-Conjugated Pyrazines as Molecularly Tunable Heterogeneous Electrocatalysts. *J. Am. Chem. Soc.* **137,** 10926–10929 (2015).

14. Heyd, J., Scuseria, G. E. & Ernzerhof, M. Hybrid functionals based on a screened Coulomb potential. *J. Chem. Phys.* **118,** 8207–8215 (2003).